OXFORD JOURNAL
OF STUDENT
SCHOLARSHIP

Optimizing Charge/Discharge Protocol for Early-Cycle Degradation in Lithium Metal Batteries

Allen Liu
allen.liu6233@gmail.com

ABSTRACT

Lithium metal anodes are often considered the "holy grail" of rechargeable, sustainable battery technology. With the highest theoretical specific capacity (3,860 mAh g^{-1}) and lowest electrochemical potential (−3.04 V vs. standard hydrogen electrode) of any metallic element, they represent the clearest path toward the next generation of higher-energy-density batteries in electric vehicles, consumer electronics, and medical devices. Their commercial adoption, however, is limited by uncontrolled lithium dendritic growth during electrochemical cycling.

This study investigates how operating temperature (room temperature vs. 35°C) and depth of discharge (DoD; Low vs. Full) influence dendrite-related degradation in Li-NMC811 CR2032 coin cells. Electrochemical impedance spectroscopy (EIS) was used to track changes in Ohmic, SEI, and charge-transfer resistance. Voltage-profile analysis and Coulombic efficiency measurements across cycling further capture how these conditions affect rate capability and the reversibility of capacity loss over time. This study seeks to move dendrite mitigation beyond the materials-level fixes that have dominated the field, toward practical, low-cost charging protocols that could be the deciding factor in whether lithium metal batteries become safe and reliable enough for widespread, real-world use.

INTRODUCTION

Historically, the efficient storage and release of energy have posed a significant hurdle to technological innovation and societal progress. In the modern era, mitigating climate change and transitioning to a decarbonized global economy demand sustainable alternatives to fossil fuels. However, because premier renewable energy sources like wind and solar are inherently intermittent, their viability relies on secondary batteries to stabilize the grid and ensure a continuous power supply. Concurrently, the development of electric vehicles (EVs) demands next-generation energy storage chemistries capable of delivering elevated energy densities alongside prolonged cycle life.

Indeed, rechargeable batteries, and specifically lithium-ion batteries (LIBs), have fundamentally transformed the energy systems industry. However, facing the growing demands for portable electronics and grid-scale energy storage, traditional LIBs with graphite and lithium cobalt oxide (LiCoO2) cathodes are unable to meet this skyrocketing growth. In particular, commercial graphite anodes approach their physicochemical limitations to reach a maximum specific energy of approximately 260 Wh kg^{-1}. This

falls well short of the >500 Wh kg^{-1} target required for next-generation EVs. Developing a high-capacity anode to replace graphite has emerged as a promising solution to boost energy density. Lithium metal is the optimal choice for the anode in high-energy-density lithium metal batteries (LMBs), because it has the highest theoretical capacity (3,860 mAh g^{-1}), lowest electrochemical potential (−3.04 V vs. standard hydrogen electrode), and lowest density (0.59 g cm^{-3}) of all possible metallic elements [1]. Furthermore, a Li metal anode is essential to Li-S and Li-air systems, both promising candidates for next-generation energy-storage applications. These advantages have positioned LMBs at the frontier for innovative electronic devices and electric vehicles (EVs).

The Lithium Dendrite Challenge

These novel Li metal anode batteries face one significant challenge: the formation of lithium dendrites. During the charging phase, Li metal electrochemically plates in an irregular manner due to inhomogeneities in the solid-electrolyte interphase (SEI), forming spiky microstructures termed "dendrites." Essentially, Li^+ ions are deposited unevenly onto the anode and develop into branching patterns, driven by the physics of rapid ion depletion and local electrical fields [2] [3]. This needle-like, metallic structure is highly destructive, as it can puncture the battery's internal separator, causing short circuits, rapid energy discharge, overheating, and fires. Dendrites also initiate a chain reaction of thermal runaway: an uncontrollable, self-sustaining reaction where a drastic increase in temperature generates cyclical heat waves. Therefore, mitigating thermal runaway and explosion risks has become a primary focus of research to ensure safe handling and distribution.

In fact, preliminary strategies have already been developed to inhibit dendritic growth [13]. For instance, solid-state electrolytes (SSEs) replace highly flammable liquid electrolytes, eliminating leakage risks while boosting energy density. However, solid-state batteries (SSBs) remain constrained by high interfacial resistance, sensitivity to mechanical stress, and prohibitive manufacturing costs. Beyond SSEs, alternative chemistries like zinc-manganese oxide (Zn-MnO2) [11] and silicon-nickel-rich layered oxide (Si-NRLO) systems [12] have been researched for their high theoretical energy densities. However, Zn-MnO2 experiences severe manganese dissolution at the cathode and pH-driven degradation within the electrolyte. Additionally, Si-NRLO expands by >300% during lithiation, which leads to unstable SEI growth and reduced Coulombic efficiency. The influence of operating temperature on lithium deposition morphology has also been investigated previously, where elevated temperatures were shown to alter transport conditions and, under certain electrolyte formulations, promote more uniform lithium deposition [8].

Research Gap and Study Rationale

Despite extensive research on lithium dendrites, the combined effects of operating conditions such as temperature and depth of discharge on degradation pathways remain incompletely understood. The majority of reports emphasize mitigating the symptoms of performance issues caused by dendrites

without addressing the root cause of their evolution and why they persist. Thus, a more in-depth and fundamental understanding of Li-dendritic formation under varying conditions is necessary.

By studying and optimizing specific charging and discharging protocols based on external variables, LMB systems can significantly prolong battery lifespan and improve overall durability. This study examines the relationship between operating temperature, depth of discharge (DoD), capacity rate (C-rate), and battery degradation metrics. Using Electrochemical Impedance Spectroscopy (EIS), we track the evolution of internal resistance metrics, such as Ohmic resistance (R1), bulk electrolyte/SEI resistance (R2), and charge-transfer resistance (R3) from Nyquist plot arcs. In doing so, we evaluate how shifting operating conditions influence battery performance during cycling and cycle life, ultimately identifying operating conditions associated with improved lifetime and safety in high-energy-density LMBs. This study hypothesizes that batteries operating at low DoD and 35°C will experience less degradation over extensive charge and discharge cycles. The higher average temperature will make the liquid electrolyte less viscous, allowing for a more uniform distribution of lithium ions before plating [5] [6]. Lower DoD, on the other hand, will reduce expansion and contraction of chemical structures, which theoretically allows battery life to be extended by an additional ~1,500-3,000 charge cycles [9] [10].

METHODS

Materials

Coin-cell batteries are the industry standard for laboratory-based experiments evaluating cathode and anode materials, binders, and electrolyte formulations. All materials, especially electrodes, separators, and electrolytes, were stored in a clean, closed environment. All tools, such as tweezers, pipettes, punches, and electrode-cutting scissors, were thoroughly checked for damage before cell assembly. Since lithium is highly reactive, cell assembly was performed in an argon-filled inert-gas glove box. Atmospheric parameters were recorded at <0.1 ppm for H2O and O2, consistent with standard practice for air- and moisture-sensitive Li-metal cell fabrication.

Cathode-active material was LiNi0.8Mn0.1Co0.1O2 (NMC811). Anode material was Li metal. Carbon black served as the conductive additive, and polyvinylidene fluoride (PVDF) was used as the polymeric binder. The active material, carbon black, and binder were combined in a weight ratio of 9:0.5:0.5 (90 wt% active material), consistent with standard coin-cell electrode formulations. The electrolyte was 1.0 M lithium hexafluorophosphate (LiPF6) dissolved in a 1:1 (v/v) mixture of ethylene carbonate (EC) and diethyl carbonate (DEC), with 2 wt% vinylene carbonate (VC) added as an SEI-stabilizing additive. A total of 75 μL of electrolyte was injected per cell to ensure adequate soaking of the electrodes. A porous, organic separator, 25 μm thick, was used to isolate the electrodes while permitting Li-ion transport. CR2032-type coin cell hardware (case, spacer, spring, cap) was used for all cells.

Electrode Preparation

The NMC811 cathode slurry was prepared by mixing the active material, carbon black, and binder in the ratio above in N-methyl-2-pyrrolidone (NMP) solvent. The slurry was then cast onto an aluminum foil current collector and dried under vacuum at 80°C for 12 hours to remove residual solvent. Cathode mass was measured for each cell to calculate areal mass loading, percent of active material, and specific capacity.

Sample	Cathode Mass (mg)
S1	14.10
S2	14.70
S3	15.30
S4	15.20

Table 1. *Cathode mass by sample.*

Theoretical specific capacity was assumed to be 200 mAh g^{-1} for NMC811. Based on the 13 mm punch diameter (electrode area = 1.327 cm^2) and 90% active-material fraction, calculated areal cathode capacities ranged from 1.91 to 2.08 mAh cm^{-2} across the four cells (Table 2). The resulting negative-to-positive (N/P) capacity ratio was approximately 25:1 to 27:1 across cells.

Sample	Active Mass (mg)	Cathode Cap. (mAh)	Areal Cap. (mAh cm^{-2})	N/P Ratio
S1	12.69	2.54	1.91	~27:1
S2	13.23	2.65	1.99	~26:1
S3	13.77	2.75	2.08	~25:1
S4	13.68	2.74	2.06	~25:1

Table 2. *Calculated areal capacity and N/P ratio by sample.*

Coin Cell Assembly

All cell components were flushed five times in the exchanger with argon. Cells were assembled in the following stacking order: negative case (cap), stainless steel spacer, lithium metal (anode), liquid electrolyte, separator, NMC811 (cathode), stainless steel spacer, spring, positive case (cap), following the standard CR2032 assembly sequence.

Assembled cells were sealed using an electric hydraulic coin-cell crimper at 1,000 psi for one crimp cycle. Following crimping, the finished cells were handled using plastic tweezers. Excess electrolyte leaking from the sides of the cell was cleaned using paper wipes. Cells were then placed in a stainless-steel holding container and exchanged with argon five times. Following crimping, cells were rested for 1 hour before testing to allow full electrolyte soaking of the separator/electrode interfaces. Cells were built per condition to account for quality of lithium, percent of active material, and mass variability between cells.

Experimental Design

This study used a 2×2 full-factorial design (temperature × DoD), with C-rate applied as a stepped secondary variable, to evaluate the independent and combined effects of operating temperature and DoD on dendrite formation and cell degradation. Prior reports have shown that both temperature and DoD are drivers of capacity fade and interfacial resistance in Li-based cells [10] [14]. Four experimental groups were defined:

Sample	Temperature	Depth of Discharge
S1	Room Temperature (20°C)	Low DoD
S2	Room Temperature (20°C)	Full DoD
S3	Elevated (35°C)	Low DoD
S4	Elevated (35°C)	Full DoD

Table 3. *Four experimental groups defined by temperature and depth of discharge.*

Due to material and time constraints, only one cell was tested under each experimental condition (n = 1). Consequently, the four samples (S1-S4) should be interpreted as individual-case observations rather than

replicated populations. Throughout this study, comparisons are presented descriptively and should be interpreted accordingly.

Independent Variables: C-rate (0.1, 0.2, 0.5, 1.0, 2.0). Operating temperature was controlled using the Neware temperature chamber, with a tolerance of ±0.5°C. Depth of Discharge:

- Low DoD = ~37.5-87.5% DoD per cycle, corresponding to a voltage window of 3.2–4.0 V
- Full DoD = 0-100% DoD per cycle, corresponding to a voltage window of 2.6–4.2 V

Dependent Variables: SEI resistance (R2) and charge-transfer resistance (R3), voltage (V), capacity (mAh), capacity retention (%) vs. cycle number, and Coulombic efficiency (%).
Control Variables: electrode composition, mass loading, cell hardware, electrolyte formulation, and electrolyte volume.

Electrochemical Cycling Protocol

Galvanostatic charge/discharge cycling was performed on a Neware MHW-25-S benchtop temperature chamber interfaced with a Neware battery cycler. Cells were cycled between 2.6 V and 4.2 V, using a CC-CV (constant-current constant-voltage, C/20 current cutoff) charge step followed by a constant-current (CC) discharge step. An initial cycle at a reduced rate (0.1 C) was performed to stabilize the SEI prior to collecting degradation data.

Cells were cycled for 28 cycles per condition (approximately 10–14 days, depending on the applied C-rate), following a stepped-C-rate protocol: cycles 1-5 at 0.1 C (baseline stability assessment), cycles 6–10 at 0.2 C, cycles 11-15 at 0.5 C, cycles 16-20 at 1 C, cycles 21-25 at 2 C, and cycles 26-28 as a recovery step returned to 0.1 C to assess baseline capacity changes. Rest periods were applied as follows: 1 minute at RT and 1 hour at 35°C between cycling steps, to allow for thermal equilibration.

Electrochemical Impedance Spectroscopy (EIS)

EIS measurements were performed using a BioLogic VMP-300 galvanostat over a frequency range of 1 Hz to 100 kHz, with an amplitude of 10 mV. Measurements were taken after every 5 cycles (coinciding with each C-rate step transition), at end-of-test, and at each DoD condition (fully charged state for Low DoD groups; fully discharged state for Full DoD groups). Nyquist plots (Zreal vs. Zimag) were fitted to an equivalent electrical circuit model consisting of L1-R1-Q2/R2-Q3/R3-Wd1. Fitting was performed using BioLogic EC-Lab software with a reported fit quality of <5% error.

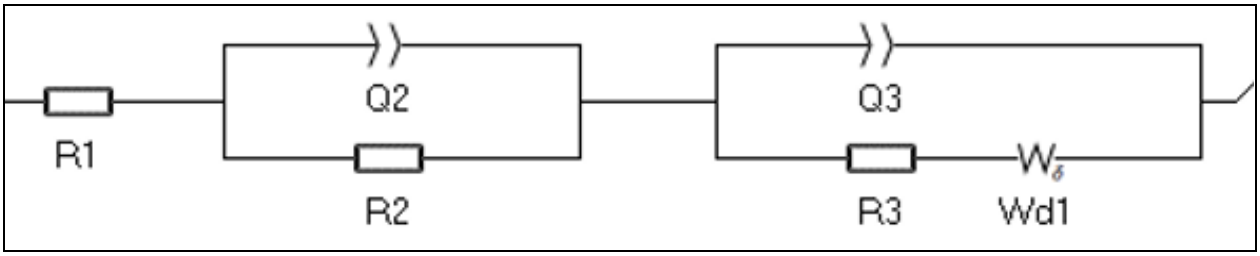


Figure 1. *Equivalent circuit model for EIS data fitting and resistance extraction.*

Data Analysis

Coulombic efficiency (CE) was calculated for each cycle as:

$$CE\ (\%) = (\text{Discharge capacity} / \text{Charge capacity}) \times 100$$

Capacity retention was defined relative to the initial baseline (average of cycles 1–10) as:

$$\text{Capacity Retention}\ (\%) = (\text{Discharge capacity} / \text{Discharge capacity baseline}) \times 100$$

Changes in R2 (SEI resistance) and R3 (charge-transfer resistance) were tracked across cycling to identify degradation trends specific to each temperature/DoD condition, following an approach consistent with prior EIS studies that correlate resistance growth with decreases in capacity [4] [14]. Voltage profiles (cell voltage vs. specific galvanic capacity) were extracted for select experimental groups (S1, S2) to characterize rate-dependent polarization behavior.

RESULTS

Electrochemical impedance spectroscopy was used to separate total cell resistance into its constituent elements. This approach enabled quantification of individual degradation mechanisms rather than relying on aggregate capacity analysis alone. In the equivalent circuit model (L1-R1-Q2/R2-Q3/R3-Wd1): R1 corresponds to resistance from the liquid electrolyte (bulk/Ohmic resistance); R2 corresponds to resistance from the SEI layer; R3 corresponds to resistance from charge moving across the electrode/electrolyte interface (charge-transfer resistance); and Wd1 corresponds to resistance from Li-ion diffusion within the electrode (Warburg element). Because dendrite formation and SEI degradation drastically manifest in R2 and R3, these parameters are most indicative of battery health and performance. Thus, R2 and R3 values, in particular, were selected for more in-depth analysis and relative Ohmic resistance comparison.

SEI and Charge-Transfer Resistance Evolution (R2, R3)

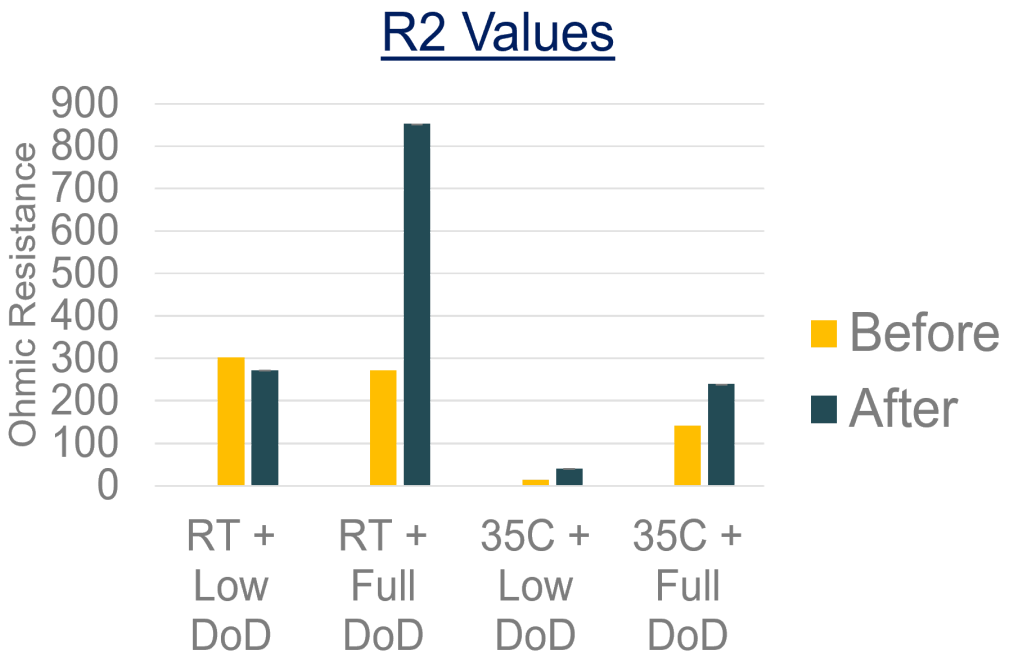


Figure 2. *Equivalent circuit model - R2 (SEI resistance) values before and after cycling, by condition.*

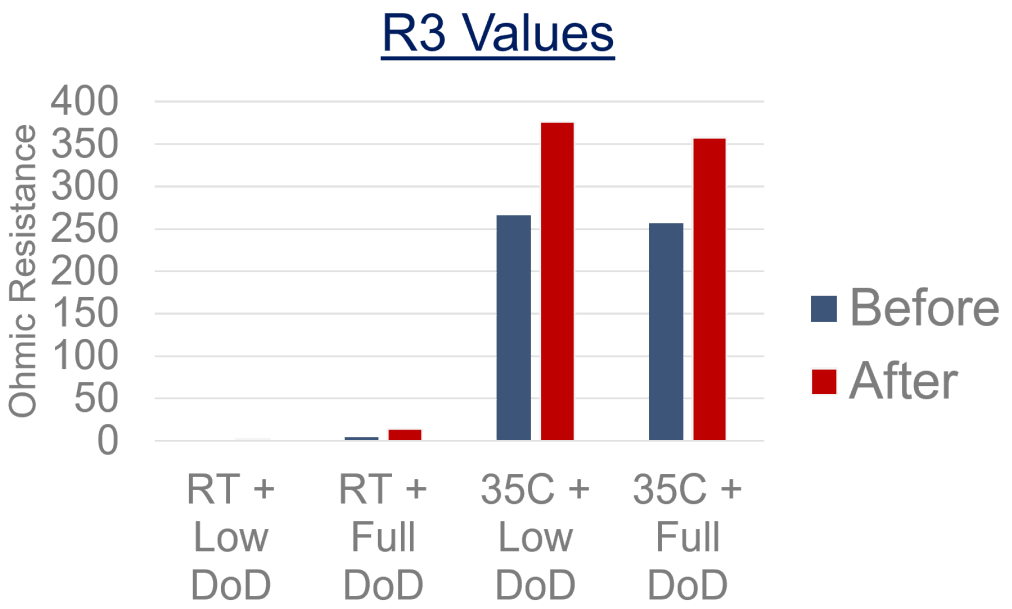


Figure 3. *Equivalent circuit model - R3 (charge-transfer resistance) values before and after cycling, by condition.*

Condition	R2 Before (Ω)	R2 After (Ω)	R3 Before (Ω)	R3 After (Ω)
RT + Low DoD	301.94	272.45	0.0050159	1.3746
RT + Full DoD	271.74	852.48	4.2936	13.783
35°C + Low DoD	14.212	40.597	265.82	376.20
35°C + Full DoD	141.45	239.45	256.92	375.24

Table 4. *Exact fitted R2 and R3 values before and after cycling.*

The R2/R3 data reveal a temperature-dependent shift in the dominant resistance pathway. At room temperature, R2 (SEI resistance) is the dominant impedance term, while R3 (charge-transfer resistance) is negligible (0.005–13.783 Ω) both before and after cycling. Within the room-temperature groups, Full DoD cycling drove a 3.14-fold increase in R2 (271.74 → 852.48 Ω) — the single largest resistance change observed across the entire dataset. In contrast, Low DoD cycling at room temperature showed R2 slightly decreased (301.94 → 272.45 Ω). This is consistent with the study's core hypothesis: repeated full depth-of-discharge promotes localized ion depletion consistent with Sand's time, the diffusion-limited point at which surface ion concentration approaches zero and dendrite nucleation becomes favorable, resulting in irregular SEI regrowth.

At 35°C, the pattern inverts: R3 (charge-transfer resistance) is the dominant and fastest-growing term (256.92–376.20 Ω), while R2 remains comparatively small (14.212–239.45 Ω). 35°C conditions showed R3 growth of similar magnitude (~42-46%), while 35°C + Full DoD additionally carried the highest absolute R2 of the two elevated-temperature groups (141.45 → 239.45 Ω), indicating that Full DoD still accelerates degradation even when temperature reduces electrolyte viscosity.

Taken together, these results suggest that elevated temperature does not eliminate degradation, as originally hypothesized, but instead redistributes it from an SEI pathway (room temperature) to a charge-transfer pathway (35°C). Full DoD cycling at room temperature produced the most severe single resistance signature (R2 = 852.48 Ω), EIS-based signatures consistent with dendrite-associated degradation. These observations should be interpreted as trends exhibited by the tested cells rather than statistically validated effects of temperature or depth of discharge. Nevertheless, the magnitude and consistency of the impedance differences suggest that the underlying degradation pathways warrant further investigation through replicated testing.

Voltage Profile Characteristics

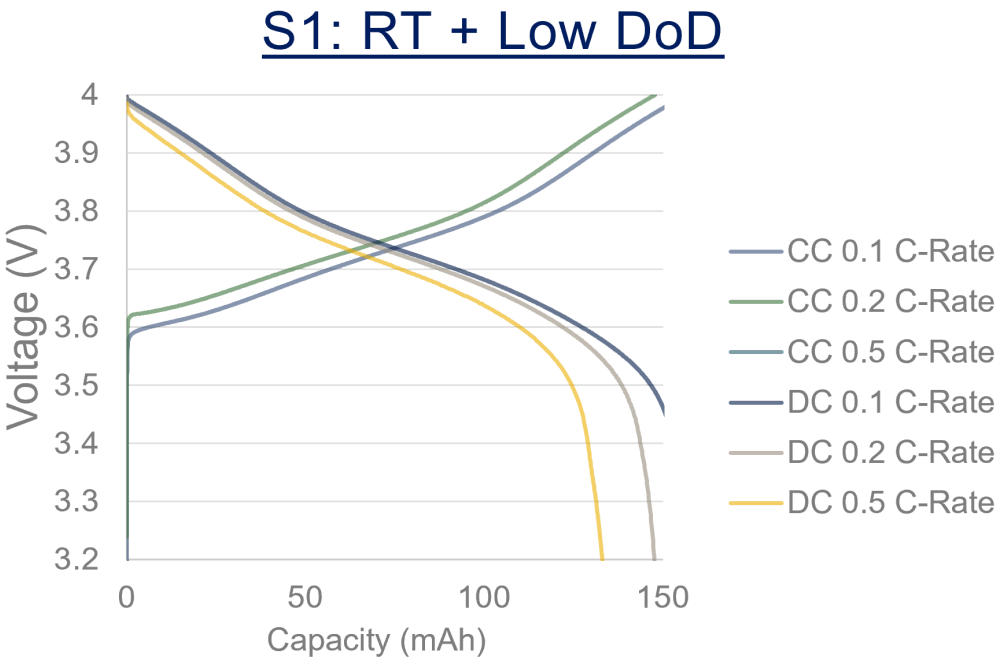


Figure 4. *Voltage vs. capacity profiles, S1 (RT + Low DoD), for CC charge and DC discharge at 0.1, 0.2, and 0.5 C.*

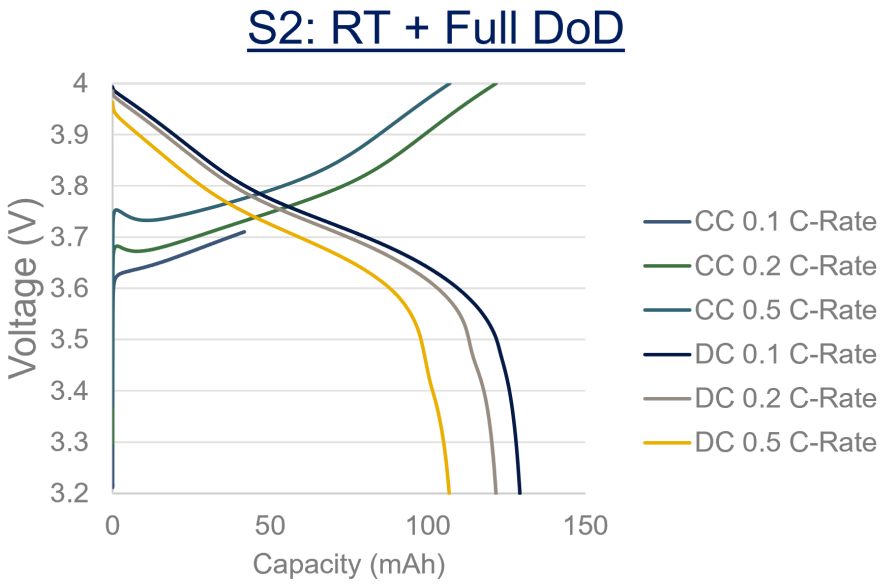
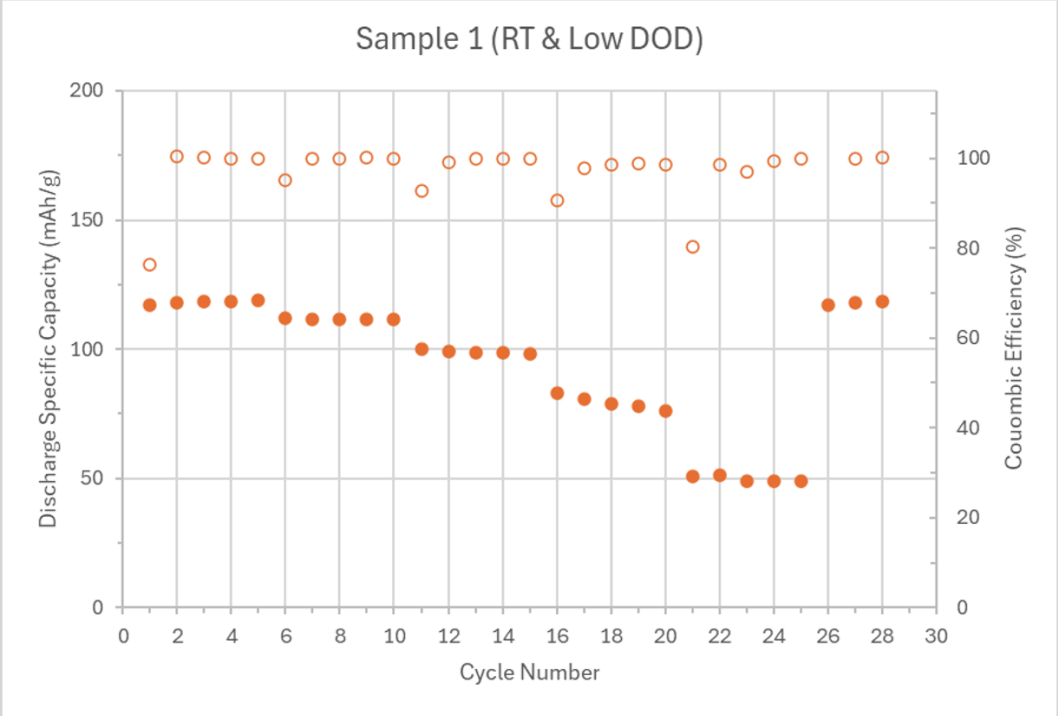


Figure 5. *Voltage vs. capacity profiles, S2 (RT + Full DoD), for CC charge and DC discharge at 0.1, 0.2, and 0.5 C.*

Voltage profiles for S1 (RT + Low DoD, Fig. 4) show tightly overlapping charge and discharge branches across all three C-rates, converging near 3.7 V at mid-capacity: the characteristic open-circuit-like crossover of a well-behaved NMC811 layered cathode. Cells reach a full capacity of approximately 150 mAh g^{-1} with only modest rate-dependent polarization; the 0.5 C discharge branch shows the earliest voltage roll-off (~130 mAh g^{-1}), but overall hysteresis between charge and discharge remains narrow, indicative of low interfacial resistance.

By contrast, S2 (RT + Full DoD, Fig. 5) shows a markedly wider separation between charge and discharge branches, particularly at low state-of-charge, and a reduced maximum capacity (~125–130 mAh g^{-1} vs. ~150 mAh g^{-1} for S1). The 0.5 C discharge curve for S2 terminates earliest (~100 mAh g^{-1}) with a sharper voltage drop, reflecting greater internal resistance limiting rate capability. This larger hysteresis and reduced accessible capacity are directly consistent with the elevated R2 (SEI resistance) measured via EIS for the RT + Full DoD condition, reinforcing that full-depth cycling at room temperature introduces meaningfully more polarization than shallow cycling under otherwise identical conditions.

Rate Capability & Cycling Stability



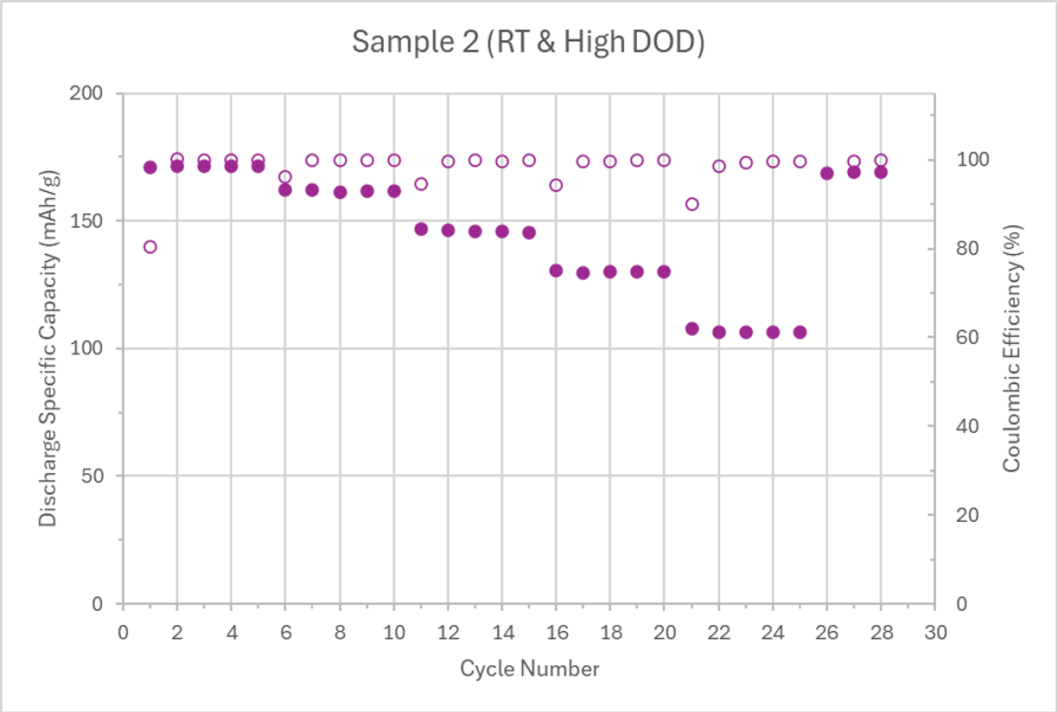
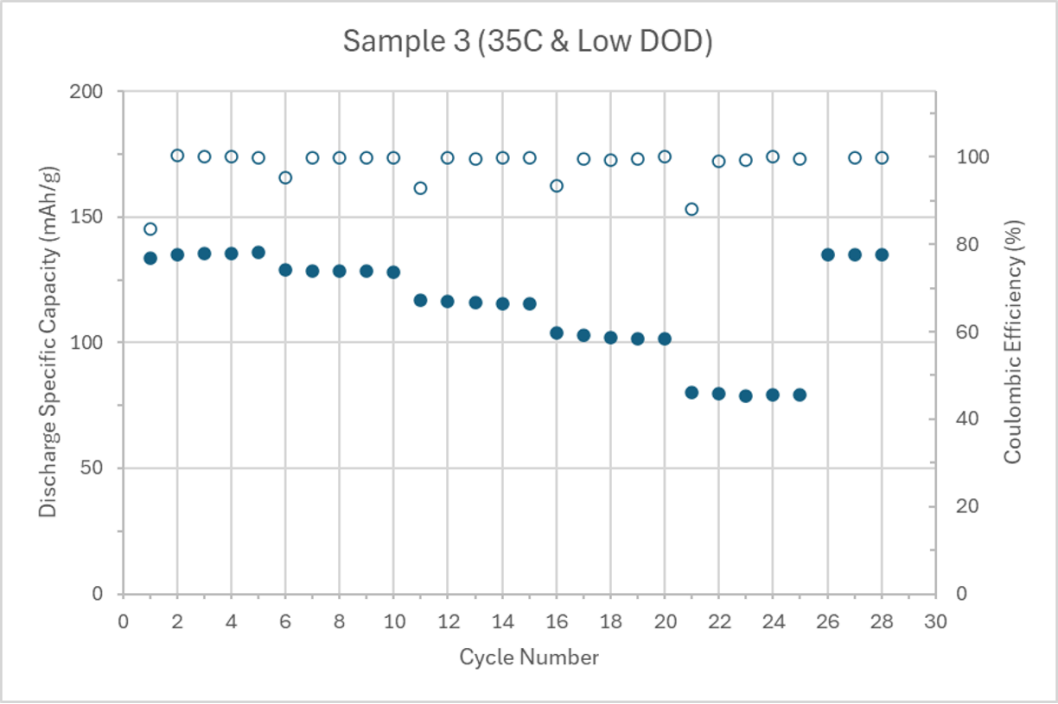


Figure 6 (top). *Sample 1, RT + Low DoD.* ***Figure 7 (bottom).*** *Sample 2, RT + Full (High) DoD. Filled markers: discharge specific capacity (left axis). Open markers: Coulombic efficiency (right axis).*



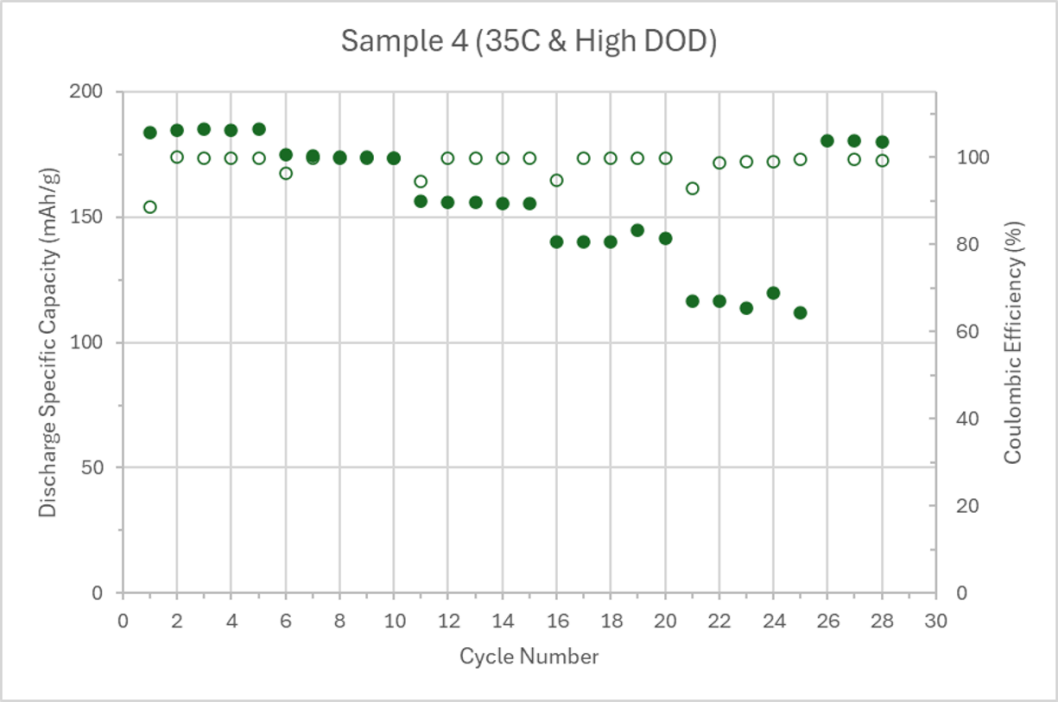


Figure 8 (top). *Sample 3, 35°C + Low DoD.* ***Figure 9 (bottom).*** *Sample 4, 35°C + Full (High) DoD.*

All four samples show the same qualitative pattern across the 28-cycle stepped-C-rate protocol: a stable baseline capacity for cycles 1–10 (0.1 C), progressive capacity decline as C-rate increases through cycles 6-25 (0.2 → 0.5 → 1.0 C → 2.0 C), and a return toward baseline capacity during the recovery segment (cycles 26–28, back to 0.1 C). Because C-rate changes within each condition, most of the apparent "fade" during cycles 11–25 reflects rate-limited kinetics rather than permanent degradation; the recovery segment is therefore the more reliable indicator of irreversible capacity loss.

Sample / Condition	**Baseline Cap. (mAh g^{-1}, cyc. 1–10)**	**Recovery Cap. (mAh g^{-1}, cyc. 26–28)**	**Recovery vs. Baseline**
S1: RT + Low DoD	~118	~119	~100%
S2: RT + Full DoD	~170	~170	~100%
S3: 35°C + Low DoD	~131	~135	~103%
S4: 35°C + Full DoD	~183	~178	~97%

Table 5. *Baseline vs. recovery discharge capacity by sample, read from Figures 6–9.*

Three of four conditions (S1, S2, S3) recovered to ≥100% of baseline capacity following the high-rate segment, indicating that within this 28-cycle window, capacity fade in those conditions was essentially fully reversible and rate-limited rather than driven by permanent active-material or lithium-inventory loss. S4 (35°C + Full DoD) was the only condition to show measurable permanent capacity loss (~3% below baseline), consistent with it also carrying the highest absolute R3 growth and the second-highest R2 among the four conditions — i.e., the combination of elevated temperature and full-depth cycling compounds both principal resistance pathways simultaneously.

Coulombic efficiency (CE) remained high (95–100%) for all conditions during steady-state segments, with characteristic dips at the first cycle of each new C-rate step (formation/equilibration transients) and a more pronounced dip around cycles 20–21 in the higher-DoD samples (S2, S4). Notably, capacity retention data alone would suggest that all four conditions are performing acceptably after only 28 cycles; it is the EIS data, not the capacity data, that first reveals the severity of degradation building in the RT + Full DoD (S2) condition. This demonstrates the value of impedance-based diagnostics as a leading indicator that precedes visible capacity fade.

As with the impedance measurements, interpretation of the cycling-performance data is limited by the lack of experimental replicates. While the recovery behavior observed in S1-S4 suggests that most performance losses during the 28-cycle protocol were rate-dependent and largely reversible, the extent to which these observations reflect generalizable trends versus cell-to-cell variability cannot be determined from the present dataset. Future studies with replicated cells will be required to quantify statistical variability and establish reproducibility.

DISCUSSION

This study set out to test the hypothesis that lithium-metal/NMC811 cells operating at low depth of discharge and 35°C would experience the least degradation during a 28-cycle electrochemical cycling protocol. The results provide partial support for this hypothesis, while revealing a more nuanced picture for temperature.

Depth of discharge appeared to be the most consistently protective variable in the present dataset: both Low DoD conditions (S1, S3) showed minimal or no growth in SEI resistance, narrow voltage hysteresis, and full recovery of capacity after high-rate cycling, regardless of temperature. Full DoD, by contrast, was implicated in the two most significant degradation signatures observed in this study: the 3.14-fold R2 growth at room temperature (S2) and the only measurable permanent capacity loss, at 35°C (S4). This supports the mechanistic rationale: repeated full-depth stripping/plating imposes greater mechanical and chemical stress on the SEI and, over longer timescales than tested here, would be expected to accelerate dendrite-driven failure.

Importantly, conclusions regarding temperature should be interpreted conservatively because only a single elevated-temperature condition (35°C) was examined. Consequently, the present study cannot determine whether the observed impedance behavior represents a broader temperature-dependent trend or a response specific to 35°C. Intermediate temperatures may exhibit substantially different electrochemical behavior, and future studies spanning a wider temperature range will be required before a generalized temperature-performance relationship can be established.

An additional limitation is the lack of replicate cells within each experimental condition. Because each condition consisted of a single cell, the observed differences cannot be separated from potential cell-to-cell variations arising from electrode loading, assembly tolerances, or localized lithium morphology. Therefore, the findings should be interpreted as identifying candidate degradation trends rather than definitive condition-dependent effects.

Temperature, however, did not behave as a simple protective factor. While elevated temperature (35°C) reduced viscosity-driven SEI resistance growth relative to room temperature, exactly as hypothesized, it simultaneously introduced a new and substantial degradation pathway through charge-transfer resistance (R3), which was substantially higher at 35°C than at room temperature from the very first measurement. In effect, elevated temperature traded one degradation mechanism for another rather than reducing degradation overall. This finding redefines the original hypothesis: operating below 35°C is not universally superior, as different resistance pathways may have different long-term failure consequences (e.g., R2 growth is more directly tied to dendrite/SEI fracture and short-circuit risk than R3 growth). A revised, more defensible interpretation emerging from this dataset is that Low DoD appears consistently protective across the tested cells, whereas increasing temperature from 20°C to 35°C alters the dominant degradation pathway rather than eliminating degradation altogether.

Future Recommendations

These conclusions are necessarily bound by the scope of this study: only one cell was tested per condition, the protocol was limited to 28 cycles, and only a single elevated temperature (35°C) was examined. The following directions would substantially extend and stress-test these findings:

Cold-Temperature Testing

Testing batteries at lower temperatures (e.g., 10°C) would allow direct examination of the electrolyte-viscosity mechanism proposed here. If SEI resistance (R2) continues to rise with decreasing temperature in a manner consistent with the RT → 35°C trend observed in this study, it would strengthen the case that viscosity-limited Li^+ transport, rather than temperature per se, is the primary driver of SEI-related degradation [5] [6].

High C-Rate Investigation

This study probed C-rates up to 2 C; investigating faster charge/discharge rates (e.g., 3–5 C) would clarify how increased current density and correspondingly faster local ion depletion influence dendrite nucleation via the Sand's time mechanism, and whether the R2/R3 partitioning observed here holds at rates more representative of fast-charging EV use cases [2] [3].

Extended Cycling

Testing to 1,000+ cycles under each of the four temperature/DoD conditions would validate whether the reversible, rate-limited capacity fade observed here eventually transitions into irreversible fade, and would allow direct correlation of long-term R2/R3 trajectories with end-of-life capacity fade and internal short-circuit incidence.

Advanced Imaging

Post-mortem SEM and optical microscopy of cycled Li-metal anodes, particularly from the RT + Full DoD (S2) and 35°C + Full DoD (S4) conditions, would enable direct correlation of R2/R3 growth with dendrite morphology, dead-lithium formation, and SEI cracking, providing physical validation of the electrochemical degradation pathways identified in this study [7] [14].

Significance & Impact

Despite these limitations, this study offers a meaningful contribution to the broader effort to understand and mitigate lithium dendrite formation. Rather than proposing another materials-level fix, this work demonstrates that operational parameters ordinarily treated as fixed, cycling temperature and depth of discharge, are themselves active levers that measurably redirect the dominant mechanism of degradation in lithium metal batteries. By modeling resistance into distinct circuit pathways, this study shows that EIS can detect the onset of condition-specific failure well before it appears as capacity fade. This reframes dendrite mitigation not solely as a materials engineering problem but also as an operational and protocol-design problem, one that can be addressed immediately and at low cost, without new coatings, additives, or electrolyte formulations. For a research community that has largely emphasized symptom-level fixes over root-cause understanding, this work provides an empirical foundation and a replicable methodology for systematically mapping the temperature–DoD design space, with direct implications for battery-management-system design in electric vehicles, consumer electronics, and safety-critical medical devices. It is this operational, mechanism-first framing, bridging fundamental interfacial electrochemistry with practical, deployable guidance, that we believe makes this study a valuable and timely addition to the lithium metal battery literature.

ACKNOWLEDGEMENTS

I would like to thank my mentor, Dr. Jinho Park, for his endless help, support, and guidance with my research and analysis into optimal charge/discharge protocols for lithium metal batteries.

AUTHOR INFORMATION

Allen Liu is a senior at Northview High School in Atlanta, Georgia. His interests span biomedical research, medicine, and engineering, with a focus on how interdisciplinary approaches can be used to solve complex problems. Through research in electrochemical energy storage and a longstanding interest in pediatric neuromuscular disease, he hopes to bridge scientific discovery and clinical care to improve patient outcomes.

REFERENCES

[1] Xu, W.; Wang, J.; Ding, F.; Chen, X.; Nasybulin, E.; Zhang, Y.; Zhang, J.-G. Lithium Metal Anodes for Rechargeable Batteries. Energy Environ. Sci. 2014, 7 (2), 513–537.

[2] Chazalviel, J.-N. Electrochemical Aspects of the Generation of Ramified Metallic Electrodeposits. Phys. Rev. A 1990, 42 (12), 7355–7367.

[3] Brissot, C.; Rosso, M.; Chazalviel, J.-N.; Lascaud, S. Dendritic Growth Mechanisms in Lithium/Polymer Cells. J. Power Sources 1999, 81–82, 925–929.

[4] Christophe, N.; Godon, A.; Thomas, A.; Lagonotte, P.; Cayzac, R. Aging Analysis of High-Capacity Graphite/NMC811 Lithium-Ion Battery Using Incremental Capacity and Electrochemical Impedance Spectroscopy. J. Electrochem. Soc. 2026, 173, 070516

[5] Petzl, M.; Danzer, M. A. Influence of Temperature and Electrolyte Composition on the Performance of Lithium Metal Anodes. Batteries 2021, 7 (4), 67.

[6] Fang, C.; Li, J.; Zhang, M.; et al. Temperature Dependence of Dendritic Lithium Electrodeposition: A Mechanistic Study of the Role of Transport Limitations within the SEI. J. Electrochem. Soc. 2020, 167 (13), 130524.

[7] Zhao, Y.; Liu, B.; Zhang, T. Effects of Key Factors on Lithium Dendrite Dissolution and Dead Lithium Formation: A Phase-Field Simulation Study. Batteries 2025, 11 (11), 413.

[8] Ding, F.; Xu, W.; Graff, G. L.; et al. Dendrite-Free Lithium Deposition via Self-Healing Electrostatic Shield Mechanism: Synergistic Effects of Salt Concentration and Working Temperature. J. Am. Chem. Soc. 2013, 135 (11), 4450–4456.

[9] Wang, X.; Zeng, W.; Hong, L.; et al. Unified Picture on Temperature Dependence of Lithium Dendrite Growth via a Phase-Field Simulation. Energy Mater. Adv. 2021, 2021, 9761464.

[10] Keil, P.; Jossen, A. Influence of Cycling Profile, Depth of Discharge and Temperature on Commercial LFP/C Cell Ageing: Post-Mortem Material Analysis of Structure, Morphology and Chemical Composition. J. Appl. Electrochem. 2020, 50, 1213–1228.

[11] Li, Y.; Wu, F.; Li, Y.; et al. Zinc-Manganese Oxide Batteries: Mechanistic Insights, Anode Engineering, and Cathode Regulation. Nanomaterials 2025, 15 (18), 1439.

[12] Wu, F.; Maier, J.; Yu, Y. Guidelines and Trends for Next-Generation Rechargeable Lithium and Lithium-Ion Batteries: Overcoming Challenges in Silicon Anodes. Chem. Soc. Rev. 2020, 49, 1569–1614.

[13] Cheng, X.-B.; Zhang, R.; Zhao, C.-Z.; Zhang, Q. Toward Safe Lithium Metal Anode in Rechargeable Batteries: A Review. Chem. Rev. 2017, 117 (15), 10403–10473.

[14] Waldmann, T.; Wilka, M.; Kasper, M.; Fleischhammer, M.; Wohlfahrt-Mehrens, M. Temperature Dependent Ageing Mechanisms in Lithium-Ion Batteries – A Post-Mortem Study. J. Power Sources 2014, 262, 129–135.